

# Active Damping of Rotating Positioning Platforms using Force Feedback

T. Dehaeze<sup>1,3</sup>, C. Collette<sup>1,2</sup>

<sup>1</sup> Precision Mechatronics Laboratory  
University of Liege, Belgium

<sup>2</sup> BEAMS Department  
Free University of Brussels, Belgium

<sup>3</sup> European Synchrotron Radiation Facility  
Grenoble, France e-mail: [thomas.dehaeze@esrf.fr](mailto:thomas.dehaeze@esrf.fr)

## Abstract

Abstract text to be done

## 1 Introduction

Due to gyroscopic effects, the guaranteed robustness properties of Integral Force Feedback do not hold. Either the control architecture can be slightly modified or mechanical changes in the system can be performed. This paper has been published The Matlab code that was use to obtain the results are available in [1].

## 2 Dynamics of Rotating Positioning Platforms

### 2.1 Model of a Rotating Positioning Platform

In order to study how the rotation of a positioning platforms does affect the use of force feedback, a simple model of an X-Y positioning stage on top of a rotating stage is developed. The model is schematically represented in Figure 1 and forms the simplest system where gyroscopic forces can be studied.

The rotating stage is supposed to be ideal, meaning it induces a perfect rotation  $\theta(t) = \Omega t$  where  $\Omega$  is the rotational speed in  $\text{rad s}^{-1}$ .

The parallel X-Y positioning stage consists of two orthogonal actuators represented by three elements in parallel:

- a spring with a stiffness  $k$  in  $\text{N m}^{-1}$
- a dashpot with a damping coefficient  $c$  in  $\text{N m}^{-1} \text{s}$
- an ideal force source  $F_u, F_v$

A payload with a mass  $m$  in kg is mounted on the rotating X-Y stage.

Two reference frames are used:

- an inertial frame  $(\vec{i}_x, \vec{i}_y, \vec{i}_z)$
- a uniform rotating frame  $(\vec{i}_u, \vec{i}_v, \vec{i}_w)$  rigidly fixed on top of the rotating stage.  $\vec{i}_w$  is aligned with the rotation axis

The position of the payload is represented by  $(d_u, d_v)$  expressed in the rotating frame.

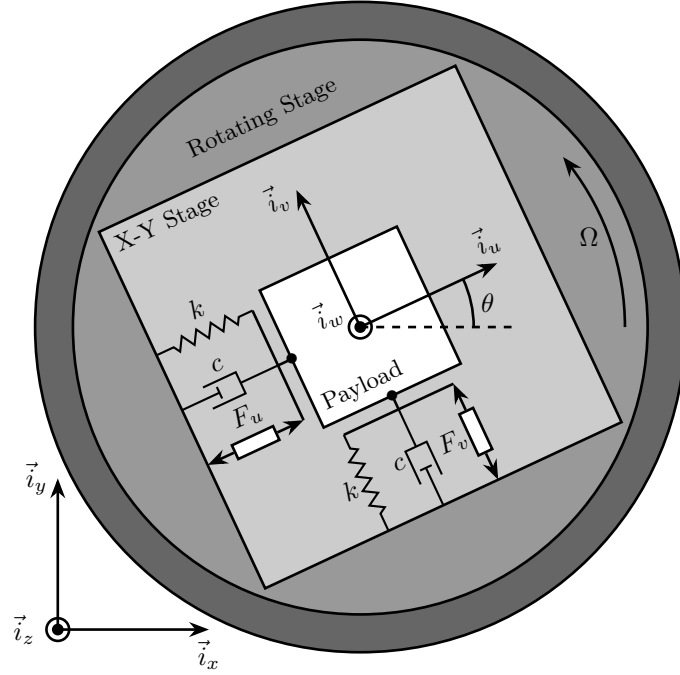


Figure 1: Schematic of the studied System

## 2.2 Equations of Motion

To obtain of equation of motion for the system represented in Figure 1, the Lagrangian equations are used:

$$\frac{d}{dt} \left( \frac{\partial L}{\partial \dot{q}_i} \right) + \frac{\partial D}{\partial \dot{q}_i} - \frac{\partial L}{\partial q_i} = Q_i \quad (1)$$

with  $L = T - V$  the Lagrangian,  $D$  the dissipation function, and  $Q_i$  the generalized force associated with the generalized variable  $[q_1 \ q_2] = [d_u \ d_v]$ .

The constant rotation in the  $(\vec{i}_x, \vec{i}_y)$  plane is here disregarded as it is imposed by the rotating stage.

$$T = \frac{1}{2} m \left( (\dot{d}_u - \Omega d_v)^2 + (\dot{d}_v + \Omega d_u)^2 \right) \quad (2a)$$

$$V = \frac{1}{2} k (d_u^2 + d_v^2) \quad (2b)$$

$$D = \frac{1}{2} c (\dot{d}_u^2 + \dot{d}_v^2) \quad (2c)$$

$$Q_1 = F_u, \quad Q_2 = F_v \quad (2d)$$

Substituting equations (2) into (1) gives the two coupled differential equations:

$$m\ddot{d}_u + c\dot{d}_u + (k - m\Omega^2)d_u = F_u + 2m\Omega\dot{d}_v \quad (3a)$$

$$m\ddot{d}_v + c\dot{d}_v + \underbrace{(k - m\Omega^2)}_{\text{Centrif.}}d_v = F_v - \underbrace{2m\Omega\dot{d}_u}_{\text{Coriolis}} \quad (3b)$$

The constant rotation of the system induces two Gyroscopic effects:

- Centrifugal forces: that can be seen as added negative stiffness along  $\vec{i}_u$  and  $\vec{i}_v$

- Coriolis Forces: that couples the motion in the two orthogonal directions

One can verify that without rotation ( $\Omega = 0$ ) the system becomes equivalent as to two uncoupled one degree of freedom mass-spring-damper systems:

$$m\ddot{d}_u + c\dot{d}_u + kd_u = F_u \quad (4a)$$

$$m\ddot{d}_v + c\dot{d}_v + kd_v = F_v \quad (4b)$$

## 2.3 Transfer Functions in the Laplace domain

To study the dynamics of the system, the differential equations of motions (3) are transformed in the Laplace domain and the  $2 \times 2$  transfer function matrix  $G_d$  from  $[F_u \ F_v]$  to  $[d_u \ d_v]$  is obtained

$$\begin{bmatrix} d_u \\ d_v \end{bmatrix} = \mathbf{G}_d \begin{bmatrix} F_u \\ F_v \end{bmatrix} \quad (5)$$

$$\mathbf{G}_d = \begin{bmatrix} \frac{ms^2+cs+k-m\Omega^2}{(ms^2+cs+k-m\Omega^2)^2+(2m\Omega s)^2} & \frac{2m\Omega s}{(ms^2+cs+k-m\Omega^2)^2+(2m\Omega s)^2} \\ -2m\Omega s & \frac{ms^2+cs+k-m\Omega^2}{(ms^2+cs+k-m\Omega^2)^2+(2m\Omega s)^2} \end{bmatrix} \quad (6)$$

To simplify the analysis, the following change of variable is performed:

- $\omega_0 = \sqrt{\frac{k}{m}}$ : Undamped natural frequency of the mass-spring system in rad/s
- $\xi = \frac{c}{2\sqrt{km}}$ : Damping ratio

The transfer function matrix (6) becomes equal to

$$\mathbf{G}_d = \frac{1}{k} \begin{bmatrix} \frac{\frac{s^2}{\omega_0^2} + 2\xi \frac{s}{\omega_0} + 1 - \frac{\Omega^2}{\omega_0^2}}{\left(\frac{s^2}{\omega_0^2} + 2\xi \frac{s}{\omega_0} + 1 - \frac{\Omega^2}{\omega_0^2}\right)^2 + \left(2\frac{\Omega}{\omega_0} \frac{s}{\omega_0}\right)^2} & \frac{2\frac{\Omega}{\omega_0} \frac{s}{\omega_0}}{\left(\frac{s^2}{\omega_0^2} + 2\xi \frac{s}{\omega_0} + 1 - \frac{\Omega^2}{\omega_0^2}\right)^2 + \left(2\frac{\Omega}{\omega_0} \frac{s}{\omega_0}\right)^2} \\ -2\frac{\Omega}{\omega_0} \frac{s}{\omega_0} & \frac{\frac{s^2}{\omega_0^2} + 2\xi \frac{s}{\omega_0} + 1 - \frac{\Omega^2}{\omega_0^2}}{\left(\frac{s^2}{\omega_0^2} + 2\xi \frac{s}{\omega_0} + 1 - \frac{\Omega^2}{\omega_0^2}\right)^2 + \left(2\frac{\Omega}{\omega_0} \frac{s}{\omega_0}\right)^2} \end{bmatrix} \quad (7)$$

For all the numerical analysis in this study,  $\omega_0 = 1 \text{ rad s}^{-1}$ ,  $k = 1 \text{ N m}^{-1}$  and  $\xi = 0.025 = 2.5\%$ . Even though no system with such parameters will be encountered in practice, conclusions will be drawn relative to these parameters such that they can be generalized to any other parameter.

## 2.4 System Dynamics and Campbell Diagram

The poles of  $G_d$  are the complex solutions  $p$  of

$$\left(\frac{p^2}{\omega_0^2} + 2\xi \frac{p}{\omega_0} + 1 - \frac{\Omega^2}{\omega_0^2}\right)^2 + \left(2\frac{\Omega}{\omega_0} \frac{p}{\omega_0}\right)^2 = 0 \quad (8)$$

Supposing small damping ( $\xi \ll 1$ ), two pairs of complex conjugate poles are obtained:

$$p_+ = -\xi\omega_0 \left(1 + \frac{\Omega}{\omega_0}\right) \pm j\omega_0 \left(1 + \frac{\Omega}{\omega_0}\right) \quad (9a)$$

$$p_- = -\xi\omega_0 \left(1 - \frac{\Omega}{\omega_0}\right) \pm j\omega_0 \left(1 - \frac{\Omega}{\omega_0}\right) \quad (9b)$$

The real part and complex part of these two pairs of complex conjugate poles are represented in Figure 2 as a function of the rotational speed  $\Omega$ . As the rotational speed increases,  $p_+$  goes to higher frequencies and  $p_-$

to lower frequencies. The system becomes unstable for  $\Omega > \omega_0$  as the real part of  $p_-$  is positive. Physically, the negative stiffness term  $-m\Omega^2$  induced by centrifugal forces exceeds the spring stiffness  $k$ .

In the rest of this study, rotational speeds smaller than the undamped natural frequency of the system are used ( $\Omega < \omega_0$ ).

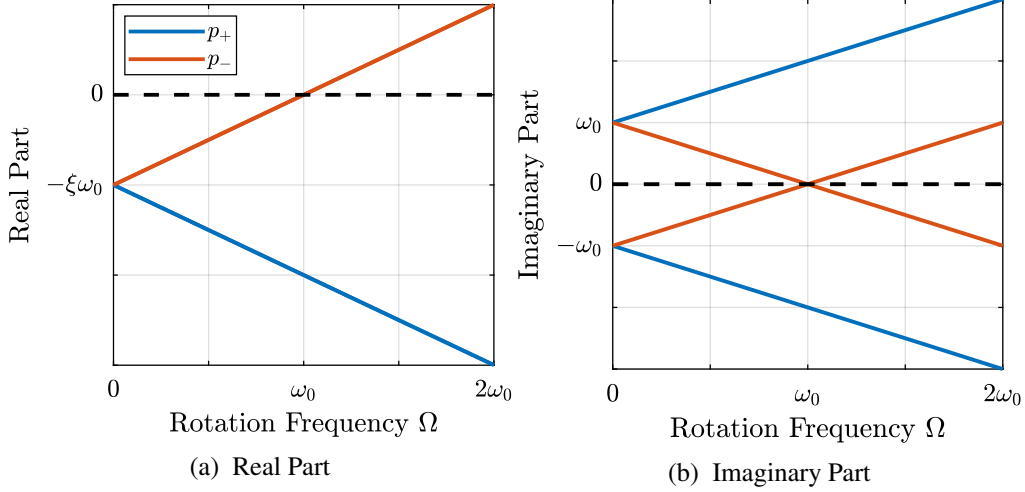


Figure 2: Campbell Diagram : Evolution of the complex and real parts of the system's poles as a function of the rotational speed  $\Omega$

Looking at the transfer function matrix  $G_d$  in Eq. (7), one can see that the two diagonal (direct) terms are equal and the two off-diagonal (coupling) terms are opposite. The bode plot of these two distinct terms are shown in Figure 3 for several rotational speeds  $\Omega$ . It is confirmed that the two pairs of complex conjugate poles are further separated as  $\Omega$  increases. For  $\Omega > \omega_0$ , the low frequency complex conjugate poles  $p_-$  becomes unstable.

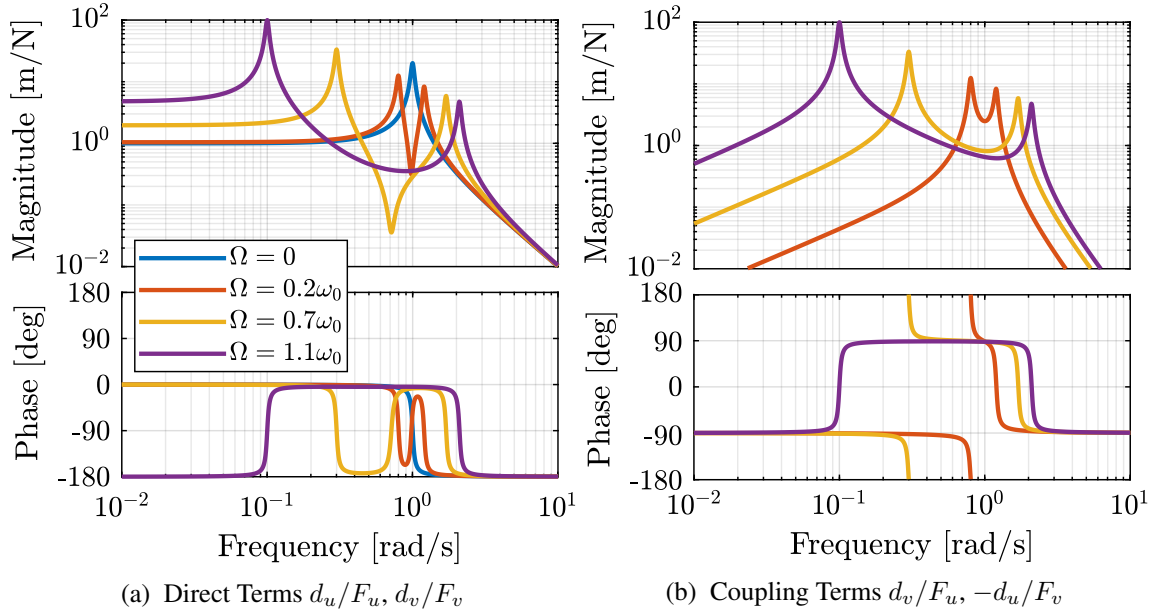


Figure 3: Bode Plots for  $G_d$  for several rotational speed  $\Omega$

### 3 Decentralized Integral Force Feedback

#### 3.1 Force Sensors and Control Architecture

In order to apply Decentralized Integral Force Feedback to the system, force sensors are added in series with the two actuators (Figure 4). Two identical controllers  $K_F$  are added to feedback each of the sensed forces to its collocated actuator. The control diagram is shown in Figure 5.

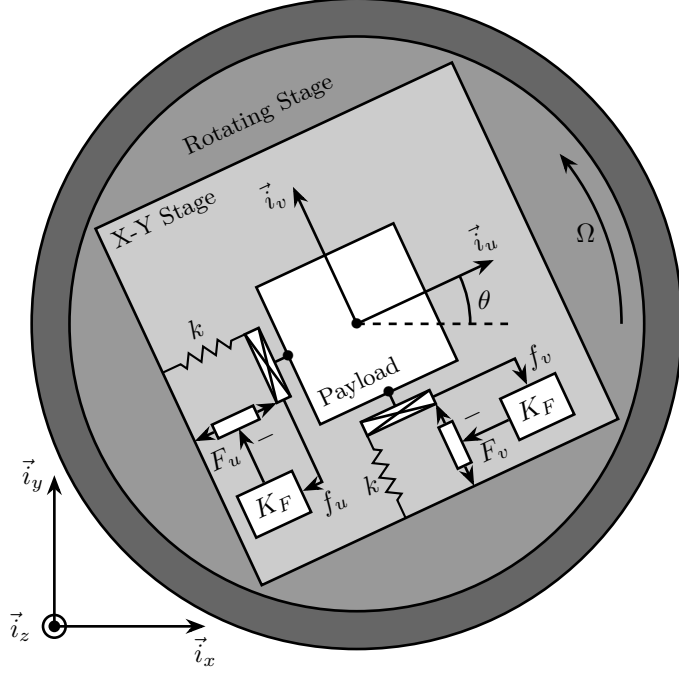


Figure 4: System with added Force Sensor in series with the actuators

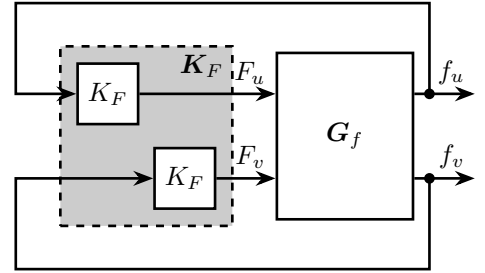


Figure 5: Control Diagram for decentralized IFF

#### 3.2 Plant Dynamics

The forces measured by the force sensors are equal to:

$$\begin{bmatrix} f_u \\ f_v \end{bmatrix} = \begin{bmatrix} F_u \\ F_v \end{bmatrix} - (cs + k) \begin{bmatrix} d_u \\ d_v \end{bmatrix} \quad (10)$$

Re-injecting (7) into (10) yields:

$$\begin{bmatrix} f_u \\ f_v \end{bmatrix} = \mathbf{G}_f \begin{bmatrix} F_u \\ F_v \end{bmatrix} \quad (11)$$

with  $\mathbf{G}_f$  a  $2 \times 2$  transfer function matrix

$$\mathbf{G}_f = \begin{bmatrix} \frac{\left(\frac{s^2}{\omega_0^2} - \frac{\Omega^2}{\omega_0^2}\right)\left(\frac{s^2}{\omega_0^2} + 2\xi\frac{s}{\omega_0} + 1 - \frac{\Omega^2}{\omega_0^2}\right) + \left(2\frac{\Omega}{\omega_0}\frac{s}{\omega_0}\right)^2}{\left(\frac{s^2}{\omega_0^2} + 2\xi\frac{s}{\omega_0} + 1 - \frac{\Omega^2}{\omega_0^2}\right)^2 + \left(2\frac{\Omega}{\omega_0}\frac{s}{\omega_0}\right)^2} & \frac{-(2\xi\frac{s}{\omega_0} + 1)\left(2\frac{\Omega}{\omega_0}\frac{s}{\omega_0}\right)}{\left(\frac{s^2}{\omega_0^2} + 2\xi\frac{s}{\omega_0} + 1 - \frac{\Omega^2}{\omega_0^2}\right)^2 + \left(2\frac{\Omega}{\omega_0}\frac{s}{\omega_0}\right)^2} \\ \frac{\left(2\xi\frac{s}{\omega_0} + 1\right)\left(2\frac{\Omega}{\omega_0}\frac{s}{\omega_0}\right)}{\left(\frac{s^2}{\omega_0^2} + 2\xi\frac{s}{\omega_0} + 1 - \frac{\Omega^2}{\omega_0^2}\right)^2 + \left(2\frac{\Omega}{\omega_0}\frac{s}{\omega_0}\right)^2} & \frac{\left(\frac{s^2}{\omega_0^2} - \frac{\Omega^2}{\omega_0^2}\right)\left(\frac{s^2}{\omega_0^2} + 2\xi\frac{s}{\omega_0} + 1 - \frac{\Omega^2}{\omega_0^2}\right) + \left(2\frac{\Omega}{\omega_0}\frac{s}{\omega_0}\right)^2}{\left(\frac{s^2}{\omega_0^2} + 2\xi\frac{s}{\omega_0} + 1 - \frac{\Omega^2}{\omega_0^2}\right)^2 + \left(2\frac{\Omega}{\omega_0}\frac{s}{\omega_0}\right)^2} \end{bmatrix} \quad (12)$$

The zeros of the diagonal terms are equal to (neglecting the damping for simplicity)

$$z_c = \pm j\omega_0 \sqrt{\frac{1}{2} \sqrt{8 \frac{\Omega^2}{\omega_0^2} + 1} + \frac{\Omega^2}{\omega_0^2} + \frac{1}{2}} \quad (13a)$$

$$z_r = \pm \omega_0 \sqrt{\frac{1}{2} \sqrt{8 \frac{\Omega^2}{\omega_0^2} + 1} - \frac{\Omega^2}{\omega_0^2} - \frac{1}{2}} \quad (13b)$$

The frequency of the two complex conjugate zeros  $z_c$  (13a) is between the frequency of the two pairs of complex conjugate poles  $p_-$  and  $p_+$  (9). This is the expected behavior of a collocated pair of actuator and sensor.

However for non-null rotational speeds, two real zeros  $z_r$  (13b) appear in the diagonal terms which represent a non-minimum phase behavior. This can be seen in the Bode plot of the diagonal terms (Figure 6) where the magnitude experiences an increase of its slope without any change of phase.

The low frequency gain of  $\mathbf{G}_f$  is no longer zero, and increases with the rotational speed  $\Omega$

$$\lim_{\omega \rightarrow 0} |\mathbf{G}_f(j\omega)| = \begin{bmatrix} \frac{-\Omega^2}{\omega_0^2 - \Omega^2} & 0 \\ 0 & \frac{-\Omega^2}{\omega_0^2 - \Omega^2} \end{bmatrix} \quad (14)$$

This low frequency gain can be explained as follows: a constant force induces a small displacement of the mass, which then increases the centrifugal forces measured by the force sensors.

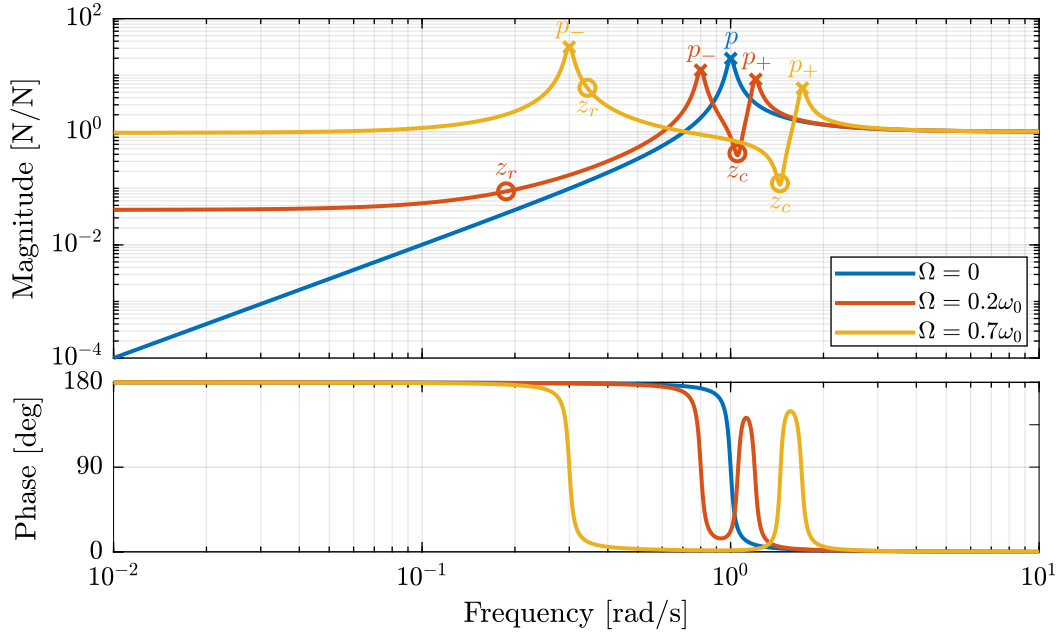


Figure 6: Bode plot of the diagonal terms of  $\mathbf{G}_f$  for several rotational speeds  $\Omega$

### 3.3 Decentralized Integral Force Feedback with Pure Integrators

The two IFF controllers  $K_F$  are pure integrators

$$\mathbf{K}_F(s) = \begin{bmatrix} K_F(s) & 0 \\ 0 & K_F(s) \end{bmatrix}, \quad K_F(s) = g \cdot \frac{1}{s} \quad (15)$$

where  $g$  is a scalar value representing the gain of the controller.

In order to see how the controller affects the poles of the closed loop system, the Root Locus is constructed as follows. The poles of the closed-loop system are drawn in the complex plane as the gain  $g$  varies from 0 to  $\infty$  for the two controllers simultaneously. The closed-loop poles start at the open-loop poles (shown by  $\times$ ) for  $g = 0$  and coincide with the transmission zeros (shown by  $\circ$ ) as  $g \rightarrow \infty$ . The direction of increasing gains is shown by the arrows  $\blacktriangleright$ .

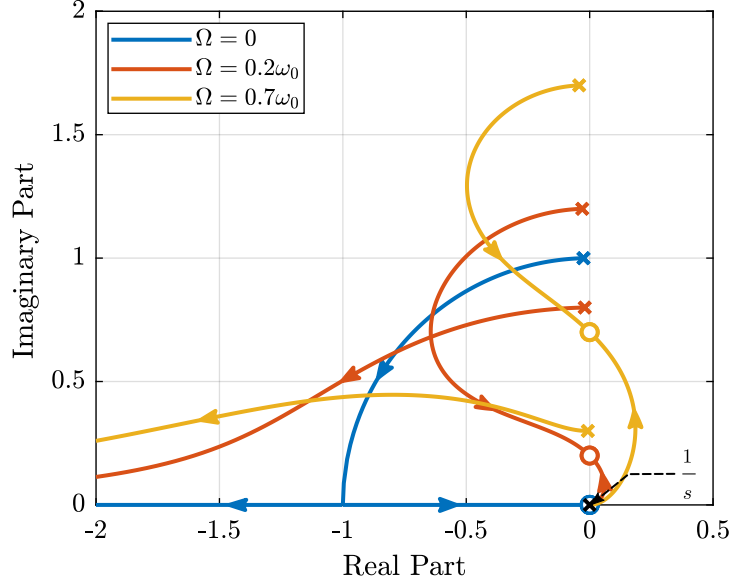


Figure 7: Root Locus for the Decentralized Integral Force Feedback

Whereas collocated IFF is known for its guaranteed stability, which is the case here for  $\Omega = 0$ , this property is lost as soon as the rotational speed is non-null due to gyroscopic effects. This can be seen in the Root Locus (Figure 7) where the pole corresponding to the controller is bounded to the right half plane implying closed-loop system instability.

Two system modifications are proposed in the next sections to deal with this stability problem. Either the control law can be changed (Section 4) or the mechanical system slightly modified (Section 5).

## 4 Integral Force Feedback with High Pass Filters

### 4.1 Modification of the Control Law

In order to limit the low frequency controller gain, a high pass filter (HPF) can be added to the controller which becomes

$$\mathbf{K}_F(s) = \begin{bmatrix} K_F(s) & 0 \\ 0 & K_F(s) \end{bmatrix}, \quad K_F(s) = g \cdot \frac{1}{s} \cdot \underbrace{\frac{s/\omega_i}{1 + s/\omega_i}}_{\text{HPF}} = g \cdot \frac{1}{s + \omega_i} \quad (16)$$

This is equivalent to slightly shifting the controller pole to the left along the real axis. This modification of the IFF controller is typically done to avoid saturation associated with the pure integrator [2]. This is however not the case in this study as it will be in the next section.

### 4.2 Feedback Analysis

The loop gains for an individual decentralized controller  $K_F(s)$  with and without the added HPF are shown in Figure 8. The effect of the added HPF is a limitation of the low frequency gain.

The Root Loci for the decentralized IFF with and without the HPF are displayed in Figure 9. With the added HPF, the poles of the closed loop system are shown to be stable up to some value of the gain  $g_{\max}$

$$g_{\max} = \omega_i \left( \frac{\omega_0^2}{\Omega^2} - 1 \right) \quad (17)$$

This gain also corresponds as to when the low frequency loop gain reaches one.

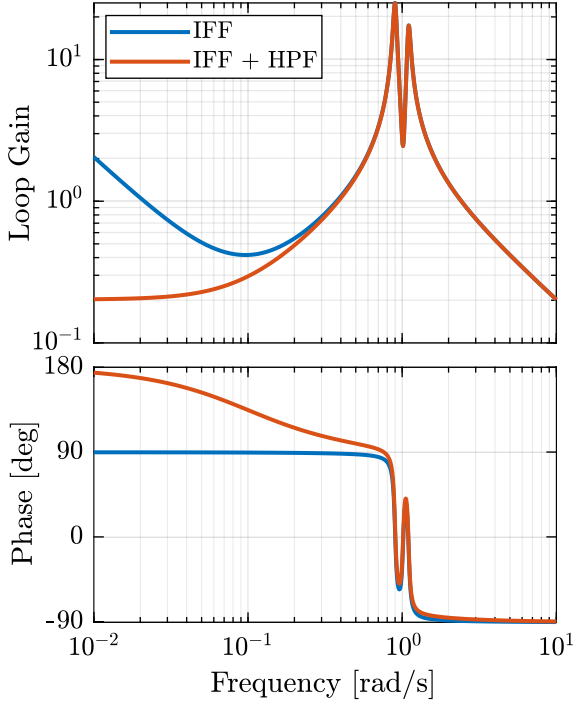


Figure 8: Modification of the loop gain with the added HFP,  $g = 2$ ,  $\omega_i = 0.1\omega_0$  and  $\Omega = 0.1\omega_0$

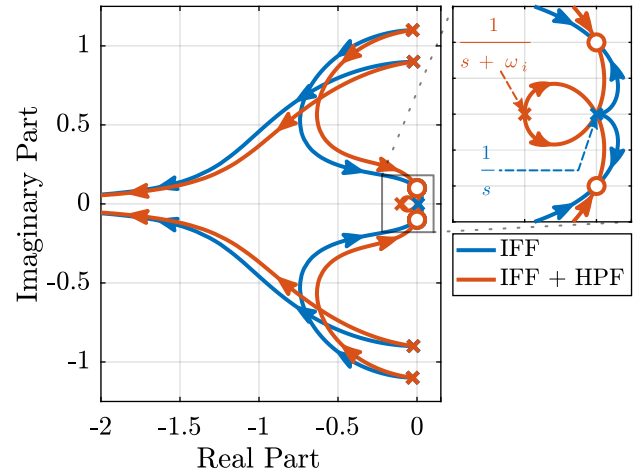


Figure 9: Modification of the Root Locus with the added HFP,  $\omega_i = 0.1\omega_0$  and  $\Omega = 0.1\omega_0$

### 4.3 Optimal Control Parameters

Two parameters can be tuned for the controller (16): the gain  $g$  and the location of the pole  $\omega_i$ . The optimal values of  $\omega_i$  and  $g$  are considered as the values for which the damping of all the closed-loop poles are simultaneously maximized.

The Root Loci for several  $\omega_i$  are shown in Figure 10. It is shown that even though small  $\omega_i$  seems to allow more damping to be added to the system resonances, the control gain  $g$  may be limited to small values due to Eq. (17).

## 5 Integral Force Feedback with Parallel Springs

### 5.1 Stiffness in Parallel with the Force Sensor

As was shown in the previous sections, the instability when using Decentralized IFF for rotating positioning platforms is due to Gyroscopic effects, more precisely to the negative stiffnesses induced by centrifugal forces. The idea in this section is to include additional springs in parallel with the force sensors to counteract this negative stiffness. Such springs are schematically shown in Figure 12 where  $k_a$  is the stiffness of the actuator and  $k_p$  the stiffness in parallel with the actuator and force sensor.

Such system could consist of additional springs, or it could also be This could represent a system where 13. The use of such amplified piezoelectric actuator for IFF is discussed in [3].

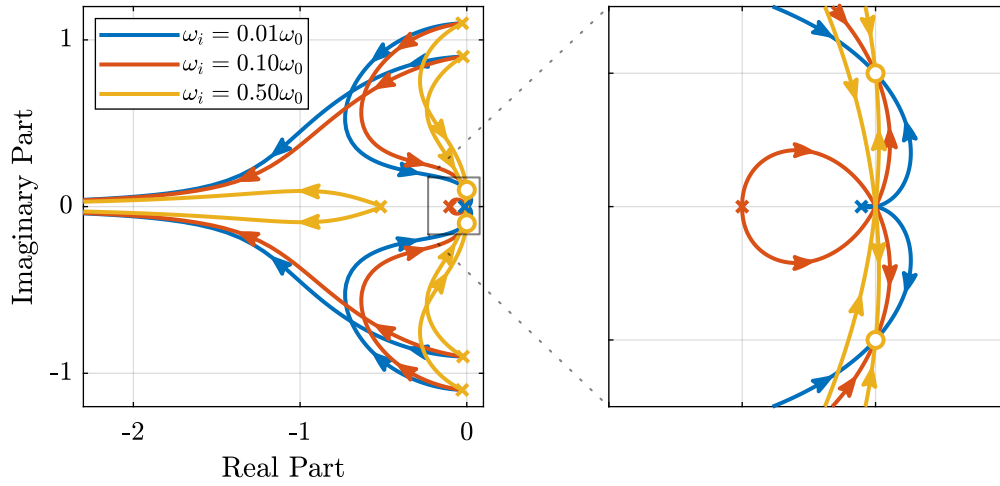


Figure 10: Root Locus for several HPF cut-off frequencies  $\omega_i$ ,  $\Omega = 0.1\omega_0$

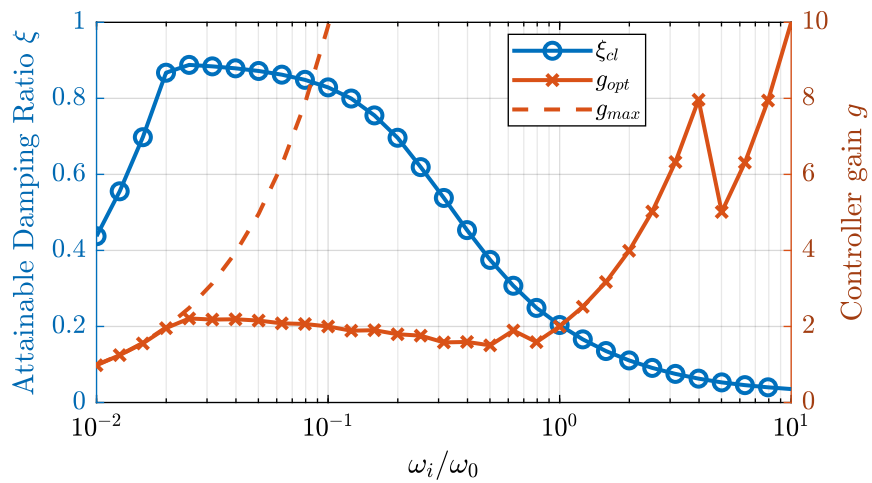


Figure 11: Attainable damping ratio  $\xi_{cl}$  as a function of the ratio  $\omega_i/\omega_0$ . Corresponding control gain  $g_{opt}$  and  $g_{max}$  are also shown

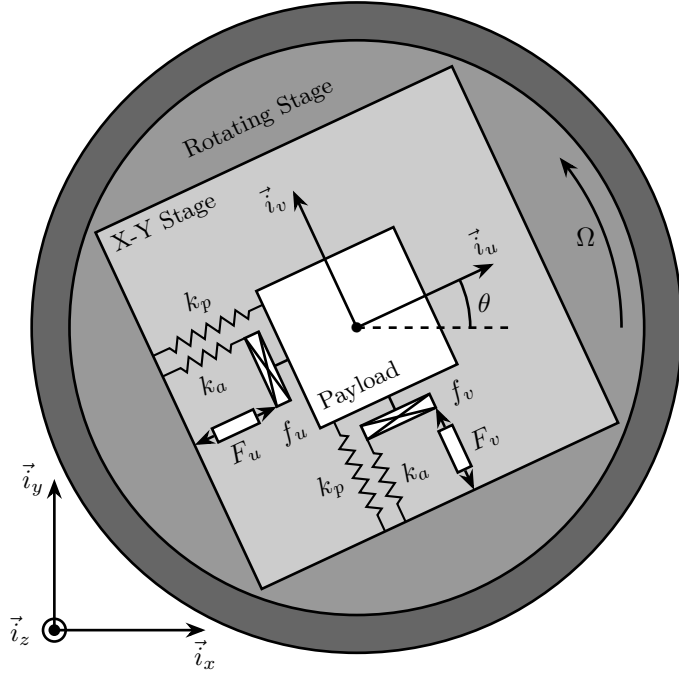


Figure 12: Studied system with additional springs in parallel with the actuators and force sensors



Figure 13: XY Piezoelectric Stage (XY25XS from Cedrat Technology)

## 5.2 Effect of the Parallel Stiffness on the Plant Dynamics

The forces measured by the sensors are equal to

$$\begin{bmatrix} f_u \\ f_v \end{bmatrix} = \begin{bmatrix} F_u \\ F_v \end{bmatrix} - (cs + k_a) \begin{bmatrix} d_u \\ d_v \end{bmatrix} \quad (18)$$

A scalar parameter  $\alpha$  ( $0 \leq \alpha < 1$ ) is defined to describe the fraction of the total stiffness in parallel with the actuator and force sensor

$$k_p = \alpha k \quad (19a)$$

$$k_a = (1 - \alpha)k \quad (19b)$$

Note that the overall stiffness  $k = k_a + k_p$  is kept constant.

The equations of motion are derived and transformed in the Laplace domain

$$\begin{bmatrix} f_u \\ f_v \end{bmatrix} = \mathbf{G}_k \begin{bmatrix} F_u \\ F_v \end{bmatrix} \quad (20)$$

with  $\mathbf{G}_k$  a  $2 \times 2$  transfer function matrix

$$\mathbf{G}_k = \begin{bmatrix} \frac{\left(\frac{s^2}{\omega_0^2} - \frac{\Omega^2}{\omega_0^2} + \alpha\right) \left(\frac{s^2}{\omega_0^2} + 2\xi \frac{s}{\omega_0} + 1 - \frac{\Omega^2}{\omega_0^2}\right) + \left(2 \frac{\Omega}{\omega_0} \frac{s}{\omega_0}\right)^2}{\left(\frac{s^2}{\omega_0^2} + 2\xi \frac{s}{\omega_0} + 1 - \frac{\Omega^2}{\omega_0^2}\right)^2 + \left(2 \frac{\Omega}{\omega_0} \frac{s}{\omega_0}\right)^2} & \frac{-(2\xi \frac{s}{\omega_0} + 1 - \alpha) \left(2 \frac{\Omega}{\omega_0} \frac{s}{\omega_0}\right)}{\left(\frac{s^2}{\omega_0^2} + 2\xi \frac{s}{\omega_0} + 1 - \frac{\Omega^2}{\omega_0^2}\right)^2 + \left(2 \frac{\Omega}{\omega_0} \frac{s}{\omega_0}\right)^2} \\ \frac{\left(2\xi \frac{s}{\omega_0} + 1 - \alpha\right) \left(2 \frac{\Omega}{\omega_0} \frac{s}{\omega_0}\right)}{\left(\frac{s^2}{\omega_0^2} + 2\xi \frac{s}{\omega_0} + 1 - \frac{\Omega^2}{\omega_0^2}\right)^2 + \left(2 \frac{\Omega}{\omega_0} \frac{s}{\omega_0}\right)^2} & \frac{\left(\frac{s^2}{\omega_0^2} - \frac{\Omega^2}{\omega_0^2} + \alpha\right) \left(\frac{s^2}{\omega_0^2} + 2\xi \frac{s}{\omega_0} + 1 - \frac{\Omega^2}{\omega_0^2}\right) + \left(2 \frac{\Omega}{\omega_0} \frac{s}{\omega_0}\right)^2}{\left(\frac{s^2}{\omega_0^2} + 2\xi \frac{s}{\omega_0} + 1 - \frac{\Omega^2}{\omega_0^2}\right)^2 + \left(2 \frac{\Omega}{\omega_0} \frac{s}{\omega_0}\right)^2} \end{bmatrix} \quad (21)$$

Comparing  $\mathbf{G}_k$  (21) with  $\mathbf{G}_f$  (12) shows that while the poles of the system are kept the same, the zeros of the diagonal terms have changed.

The two real zeros  $z_r$  (13b) that were inducing non-minimum phase behavior are transformed into complex conjugate zeros for

$$\begin{aligned} \alpha &> \frac{\Omega^2}{\omega_0^2} \\ \Leftrightarrow k_p &> m\Omega^2 \end{aligned} \quad (22)$$

Thus, if the added parallel stiffness  $k_p$  is higher than the negative stiffness induced by centrifugal forces  $m\Omega^2$ , the direct dynamics from actuator to force sensor will show minimum phase behavior. This is confirmed by the Bode plot in Figure 14.

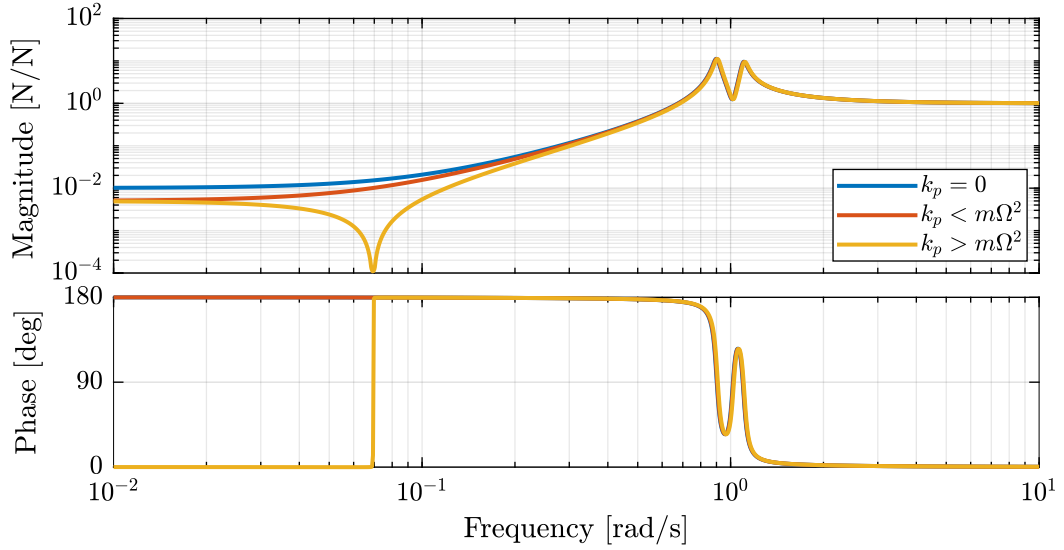


Figure 14: Bode Plot of  $f_u/F_u$  without parallel spring, with parallel springs with stiffness  $k_p < m\Omega^2$  and  $k_p > m\Omega^2$ ,  $\Omega = 0.1\omega_0$

Figure 15 shows Root Loci plots for  $k_p = 0$ ,  $k_p < m\Omega^2$  and  $k_p > m\Omega^2$  when  $K_F$  is a pure integrator (15). It is shown that if the added stiffness is higher than the maximum negative stiffness, the poles of the closed-loop system stay in the (stable) right half-plane, and hence the unconditional stability of IFF is recovered.

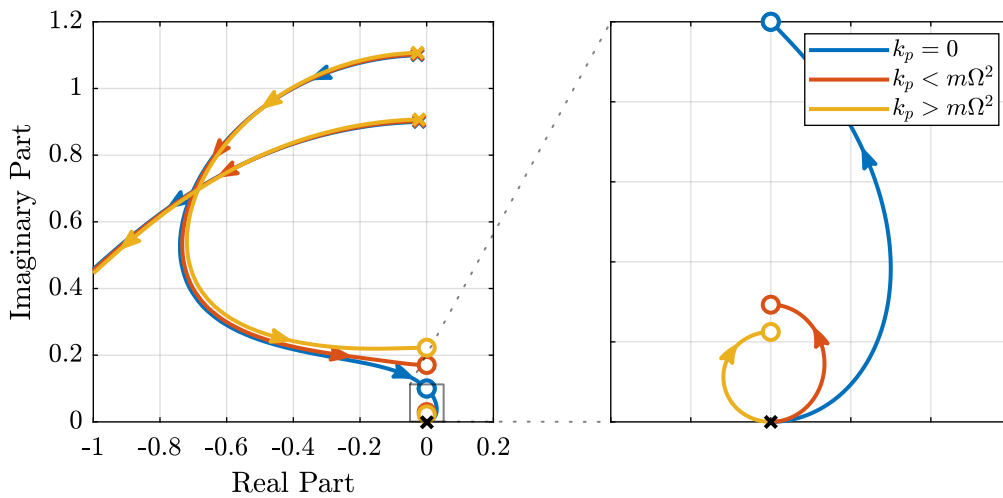


Figure 15: Root Locus for IFF without parallel spring, with parallel springs with stiffness  $k_p < m\Omega^2$  and  $k_p > m\Omega^2$ ,  $\Omega = 0.1\omega_0$

### 5.3 Optimal Parallel Stiffness

Figure 16a shows Root Loci plots for several parallel stiffnesses  $k_p > m\Omega^2$ . It is shown that large parallel stiffness  $k_p$  reduces the attainable damping. This can be explained by the fact that as the parallel stiffnesses increases, the transmission zeros are closer to the poles. As explained in [4], the attainable damping is generally proportional to the distance between the poles and zeros. The frequency of the transmission zeros of the system are increasing with the fraction used as parallel stiffness  $k_p$ .

For any  $k_p > m\Omega^2$ , the control gain  $g$  can be tuned such that the maximum simultaneous damping is added to the resonances of the system as shown in Figure 16b for  $k_p = 5m\Omega^2$ .

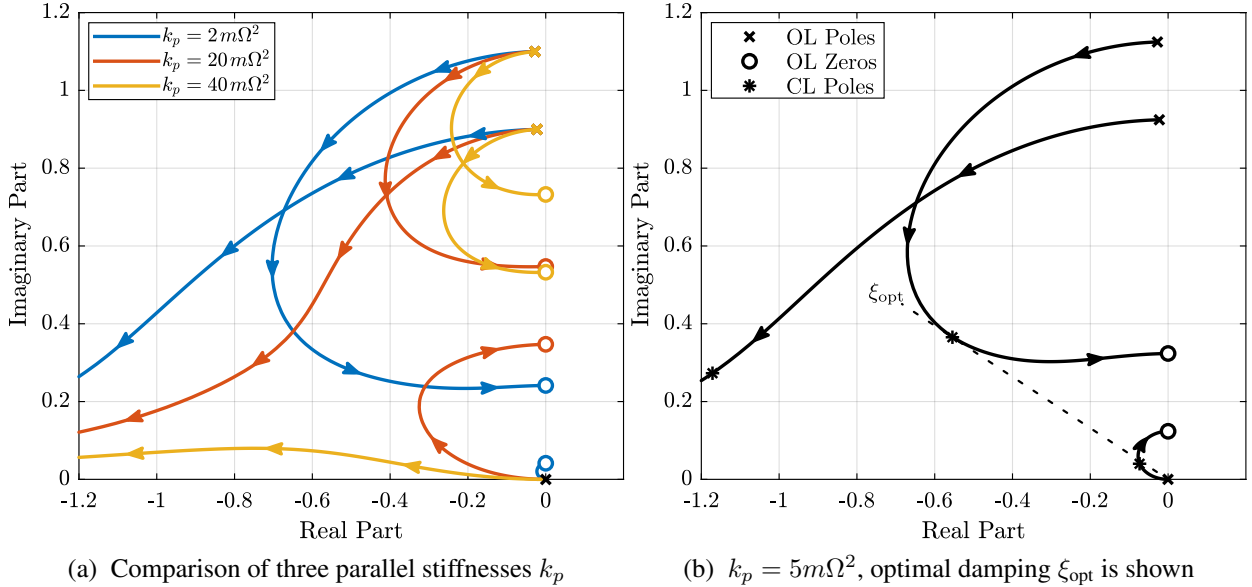


Figure 16: Root Locus for IFF when parallel stiffness  $k_p$  is added,  $\Omega = 0.1\omega_0$

## 6 Comparison of the Proposed Modification to Decentralized Integral Force Feedback for Rotating Positioning Stages

The two proposed modification to the decentralized IFF for rotating positioning stages are now compared. Two modification to the decentralized IFF for rotating positioning stages have been proposed.

The first modification concerns the controller. It consists of adding an high pass filter to  $K_F$  (16). This allows the system to be stable for gains up to  $g_{max}$  (17).

The second proposed modification concerns the mechanical system. If springs are added in parallel to the actuators and force sensors with a stiffness  $k_p > m\Omega^2$ , decentralized IFF can be applied with unconditional stability.

These two methods are now compared in terms of added damping, closed-loop compliance and transmissibility. For the following comparisons, the high pass cut-off frequency is set to  $\omega_i = 0.1\omega_0$  and the parallel stiffness is  $k_p = 5m\Omega^2$ .

### 6.1 Comparison of the Attainable Damping

Figure 17 shows to Root Locus plots for the two proposed IFF techniques. The maximum added damping is very similar for both techniques and are reached for  $g_{opt} \approx 2$  in both cases.

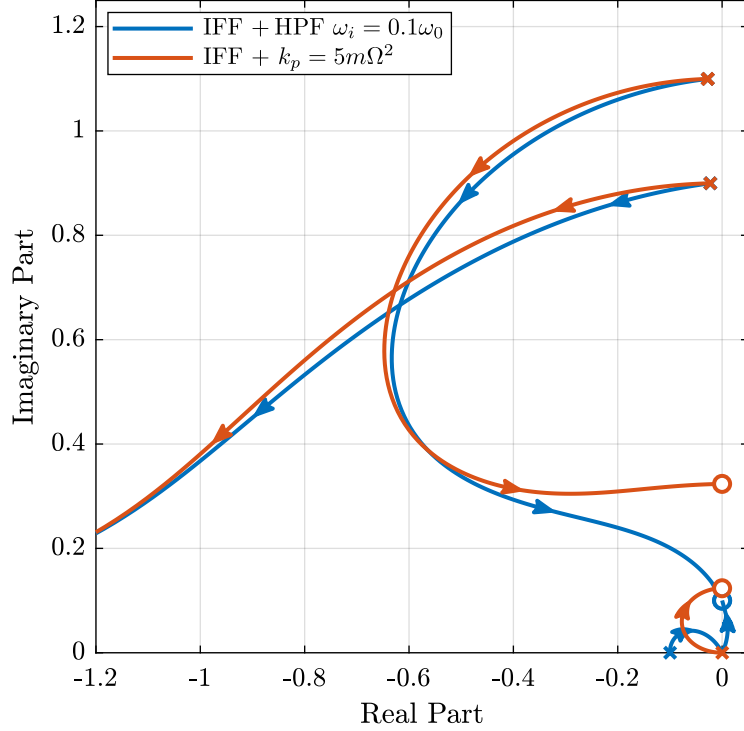


Figure 17: Root Locus for the two proposed modifications of decentralized IFF,  $\Omega = 0.1\omega_0$

## 6.2 Comparison Transmissibility and Compliance

The two proposed techniques are now compared in terms of closed-loop compliance and transmissibility.

The compliance is defined as the transfer function from external forces applied to the payload to the displacement of the payload in an inertial frame. The transmissibility is the dynamics from the displacement of the rotating stage to the displacement of the payload. It is used to characterize how much vibration of the rotating stage is transmitted to the payload.

The two techniques are also compared with passive damping (Figure 1) with  $c$  tuned to critically damp the resonance when  $\Omega = 0$

$$c_{\text{crit}} = 2\sqrt{km} \quad (23)$$

Very similar results are obtained for both techniques as shown in Figures 18a and 18b. It is also confirmed that these techniques can significantly damp the system's resonances.

Compared to passive damping, the two techniques degrades the compliance at low frequency (Figure 18a). They however do not degrades the transmissibility as high frequency as its the case with passive damping (Figure 18b)

## 7 Conclusion

### Acknowledgment

This research benefited from a FRIA grant from the French Community of Belgium.

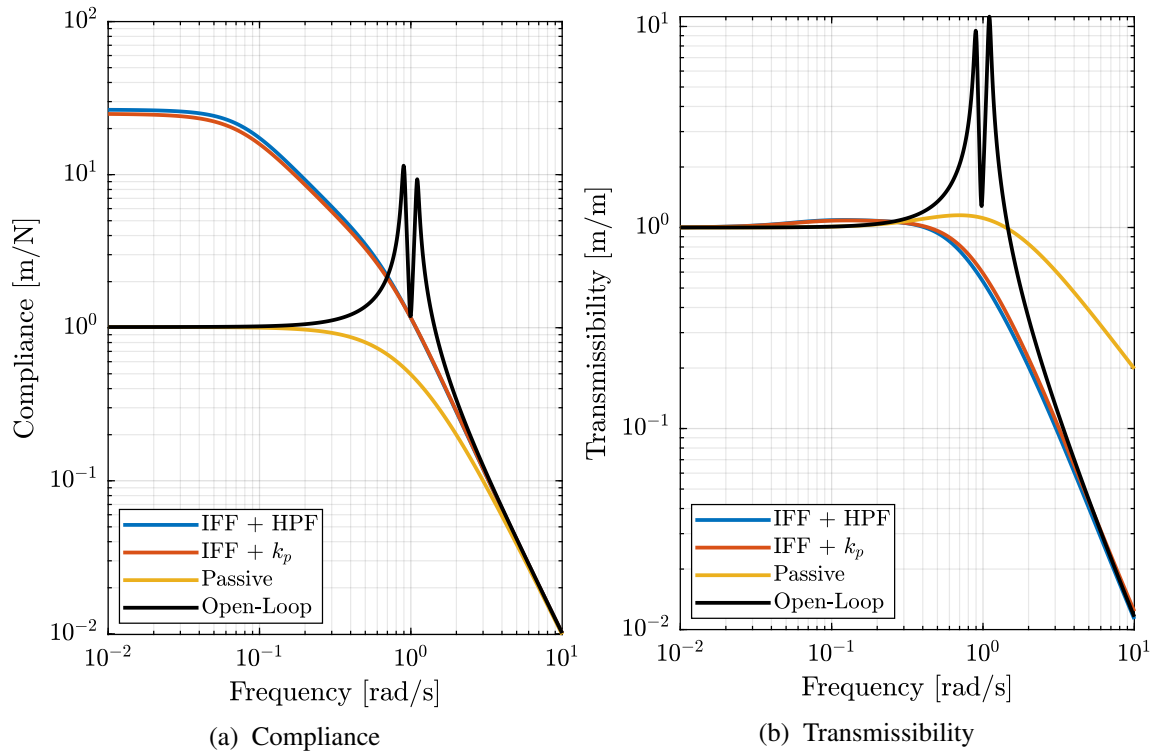


Figure 18: Comparison of the two proposed Active Damping Techniques,  $\Omega = 0.1\omega_0$

## References

- [1] T. Dehaeze, "Active damping of rotating positioning platforms," Source Code on Zonodo, 07 2020. [Online]. Available: <https://doi.org/10.5281/zenodo.3894342>
- [2] A. Preumont, J.-P. Dufour, and C. Malekian, "Active damping by a local force feedback with piezoelectric actuators," in *32nd Structures, Structural Dynamics, and Materials Conference*. American Institute of Aeronautics and Astronautics, apr 1991. [Online]. Available: <https://doi.org/10.2514/6.1991-989>
- [3] A. Souleille, T. Lampert, V. Lafarga, S. Hellegouarch, A. Rondineau, G. Rodrigues, and C. Collette, "A concept of active mount for space applications," *CEAS Space Journal*, vol. 10, no. 2, pp. 157–165, 2018.
- [4] A. Preumont, *Vibration Control of Active Structures - Fourth Edition*, ser. Solid Mechanics and Its Applications. Springer International Publishing, 2018. [Online]. Available: <https://doi.org/10.1007/978-3-319-72296-2>